A Method for Effective Permittivity and Conductivity Mapping of Biological Scenarios via Segmented Contrast Source Inversion

**Martina T. Bevacqua[1], Gennaro G. Bellizzi[1, 2],
Tommaso Isernia[1, 2, *], and Lorenzo Crocco[2]**

Abstract—Quantitative estimation of both conductivity and permittivity of biological tissues is essential in many biomedical applications, ranging from therapeutic treatments to safety assessment of medical devices and dosimetry. Typically, the electromagnetic field distribution inside the body is predicted based on available *ex-vivo* measured electrical properties. Unfortunately, these values may be quite different from the ones measured *in-vivo* and cannot account for the differences among individuals. As a result, their use can introduce significant errors affecting therapeutic treatments and dose estimation. To cope with this problem, in this paper a new approach for estimation of effective electrical properties of human tissues is introduced. The proposed strategy is based on the solution of an inverse scattering problem (by means of a contrast source inversion scheme) and the use of an effective representation of the unknowns based on spatial priors derived by magnetic resonance imaging or computed tomography. The approach is tested in controlled conditions against simulated single frequency data and realistic and anthropomorphic head and neck phantoms. Moreover, the inherent advantages have been assessed in the framework of hyperthermia treatment planning.

1. INTRODUCTION

The proper evaluation of the interaction between electromagnetic waves and the human body is nowadays increasingly important, owing to the pervasiveness of electromagnetic technologies. As a matter of fact, accurate knowledge of the field distribution is needed in dosimetry to assess the safety of human exposure to radiating devices [1], as well as in planning anti-cancer hyperthermia treatments (HTP) to deliver an optimal, patient-specific, therapy by synthesizing the excitations of the applicator [2–4]. Also, the field distribution is required for a proper design of wireless powering of implanted devices coupled from external sources [5]. On the other hand, since performing the relevant field measurements is usually not possible, field evaluation relies on numerical simulations. To this end, a key role is played by the electrical properties (EPs) of biological tissues, namely, conductivity and permittivity, whose proper knowledge is essential to build reliable computational models of the human body.

Currently, electromagnetic models are derived from medical images obtained by magnetic resonance imaging (MRI) or computed tomography (CT). By segmenting these images, a 3D spatial model with tissue labeling is generated. Then, the EPs are tissue-wise associated on the basis of the average values reported in the literature, arising from measurements of *ex-vivo* tissue samples [6, 7]. As such, the models obtained in this way assume that the EPs *in-vivo* and the ones *ex-vivo* measured are essentially the same. Unfortunately, this seems to be not the case, according to some studies showing a not

* Corresponding author: Tommaso Isernia (tommaso.isernia@unirc.it).
[1] DIIES, Department of Information Engineering, Infrastructures and Sustainable Energy, Università Mediterranea of Reggio Calabria, via Graziella, Loc. Feo di Vito, 89124, Reggio di Calabria, Italy. [2] CNR-IREA, National Research Council of Italy — Institute for Electromagnetic Sensing of the Environment, via Diocleziano 328, 80124, Napoli, Italy.

negligible difference existing between *ex-vivo* and *in-vivo* EPs [8–11]. Hence, there's an increasing need of characterizing the actual *in-vivo* EPs. In this respect, the straightforward direct and invasive measure of the *in-vivo* properties can be fallacious. First, in some cases invasive measurements are not possible, e.g., bone, bone marrow [12]. Second, in case invasive measurements are feasible, the adoption of an average inter-patients EPs values would flat the natural human body variability [13]. Therefore, an approach to estimate the *in-vivo* EPs in a non-invasive, low-cost and case-specific way is highly needed.

A possible technique could consist in a proper processing of the magnetic field acquired by an MRI system [14], thus being able to reach high accuracy in determining the complex permittivity of the scenario. However, such an approach only works at the MRI scanner resonance frequency, so that it implicitly requires that a reliable dispersion relationship is available. Moreover, the measured data are affected by phase uncertainties [15]. As an alternative, microwave tomography (MWT) [16–20] could be exploited, as this technique indeed provides a low-cost and non-invasive modality to image the inside of the human body at the frequencies of interest for the above-mentioned applications. On the other hand, it is well known that, as compared to MRI and CT, MWT exhibits a low spatial resolution, which would ultimately impair the pursued goal (i.e., high resolution mapping of the EPs to build reliable computational models).

To address such an inconvenience, in this paper, a new MWT approach for estimation of effective EPs of biological tissues is proposed and described. The approach is based on the simple idea of incorporating morphological information obtained from MRI or CT images into the MWT algorithm, in order to benefit from the high spatial resolution characterizing these images. In particular, the spatial priors derived from segmented medical images are exploited to build a patient-specific representation basis of the unknown EPs. As a result, the properties are encoded by means of a set of (complex) coefficients corresponding to the effective EPs of each tissue, as segmented from the MRI or CT map. Note that besides ensuring high resolution images, this strategy allows a dramatic reduction of the unknown parameters, which, as extensively discussed in [21], has a crucial influence on reliability and accuracy of the retrieval procedure. In practice, the inverse scattering problem, herein solved by means of a contrast source inversion (CSI) scheme [22], is turned into a parameters estimation, whose unknowns are just the effective EPs of the tissue tagging in the MRI or CT map. Also note that approximating the actual EPs distributions with a step-wise constant function is the common assumption when therapeutic treatments are planned or field exposure is quantified [1–4]. As such, the spatial regularization herein introduced belongs to the *hard prior* techniques, which can exhibit better performance with respect to the *soft prior* techniques [23], wherein the EPs inside the tissue are not enforced to be exactly step-wise constant but instead large variations are penalized [23].

The integration of MRI/CT based spatial priors (both hard and soft) into MWT has also been considered in previous studies [23–25], in the framework of breast imaging (which is indeed another application for which the method herein proposed is suitable). However, there are several significant differences between the method herein proposed and those studies. As a matter of fact, in those approaches, the spatial constraints are enforced as penalty terms within a l_2 norm regularization framework. This entails the need of weighting their contribution through properly selected regularization parameters. This circumstance, and the very large number of unknowns which is anyway dealt with, ultimately affects their effectiveness and applicability. In fact, up to now they have been proved to be effective only for over-simplified scenarios consisting of at most three biological tissues. Another example of regularization based on MRI/CT spatial priors is introduced in [26]. However, in this latter the EPs tomography is performed by processing the signal from MRI scanner by means a Newton-Kantorovich inversion scheme, which requires both the solution of several forward problems as well as the solution of several linearized inverse problems.

With respect to the above-mentioned works, the proposed technique is more flexible, as the spatial priors are herein enforced in such a way to deal with realistic anatomical heterogeneous structures, which can be made up by many different tissues. Moreover, the proposed strategy involves a much simpler implementation and higher efficiency both in terms of memory and computation, and there is no need to select regularization parameters. Finally, it is important to underline that the approach herein proposed processes single frequency data. This implies simplicity of the involved hardware and, differently from [25], no need of using dispersion relaxations which could not model with enough accuracy the *in-vivo* EPs. Indeed, the approach herein introduced could instead allow the determination

of alternative and eventually more appropriate *in-vivo* dispersion model of the investigated tissues.

From a technological point of view, the feasibility of the approach, as well as of those in [23–25], relies on the capability of co-registering MRI and CT images with the MWT system. While this may be challenging, there are already examples of devices which circumvent this difficulty in the hyperthermia treatment of head & neck (H&N) tumors [27]. Moreover, because of the need of monitoring the temperature distribution during the treatment [28], MRI-compatible microwave systems are being developed [29]. As a consequence, one could have a simultaneous acquisition of MRI and microwave signals.

The paper is organized as follows. In Section 2, the basics of the inverse scattering problem are recalled together with the role of the representation basis. In Section 3, the proposed MRI/CT based projection and the Segmented CSI scheme are introduced and described. In Section 4, a 'controlled' numerical assessment is carried out against a 2D H&N scenario, which is a challenging example of a heterogeneous biological scenario. Section 5 presents a practical example of the usefulness of the proposed approach in the framework of HTP by exploiting a recently introduced technique [30]. Finally, conclusions follow.

2. INVERSE SCATTERING PROBLEM

The inverse scattering problem amounts to recover the geometry and electromagnetic properties of unknown scattering objects starting from the knowledge of the incident fields and the measurements of the corresponding scattered fields [16]. For the sake of simplicity, let us consider the canonical 2D scalar problem (TM polarized fields) in which the scenario is invariant along one direction and the electric fields are polarized along the invariance axis. Note that all difficulties pertaining to the 3D inverse scattering problem of interest, namely non-linearity (possibly leading to false solutions [21]) and ill-posedness, are already present in the 2D geometry. Moreover, the approach introduced in the following Sections can be straightforwardly extended to the case of 3D geometries.

Let Ω denote the region of interest where the targets are located, and $\epsilon_s(\mathbf{r})$ and $\epsilon_b(\mathbf{r})$ the complex permittivities of the scatterers and the background medium, respectively, with $\mathbf{r} = (x, y)$ scanning the investigation domain Ω. This latter is probed by means of a set of incident fields transmitted by some antennas located in $\mathbf{r_t}$ on a closed curve Γ and the resulting scattered fields are measured by receiver antennas also located in $\mathbf{r_m} \in \Gamma$. For the generic transmitter, the equations describing the problem are the *data* and *state* equations [16]:

$$E_s(\mathbf{r_m}, \mathbf{r_t}) = \mathcal{A}_e[W(\mathbf{r}, \mathbf{r_t})] \tag{1}$$

$$W(\mathbf{r}, \mathbf{r_t}) = \chi(\mathbf{r})E_i(\mathbf{r}, \mathbf{r_t}) + \chi(\mathbf{r})\mathcal{A}_i[W(\mathbf{r}, \mathbf{r_t})] \tag{2}$$

where E_i, E_s and W are the incident field, the scattered field and the contrast source induced in the scatterers, respectively, and $\chi(\mathbf{r}) = \epsilon_s(\mathbf{r})/\epsilon_b(\mathbf{r}) - 1$ is the contrast function, which relates the unknown properties of the targets to those of the background medium. Finally, $\mathcal{A}_e$ and $\mathcal{A}_i$ are short notations for the corresponding integral radiation operators (see [16, 17] for more details). As well-known, the problem (1)–(2) is non-linear, as the contrast sources W also depend on the unknown of the problem, i.e., the contrast function χ. Moreover, it is also ill-posed due to the properties of the involved operator $\mathcal{A}_e$ [17]. In order to face such difficulties, different efforts have been made in literature in order to develop effective and reliable approaches. For our purposes, among the different regularization techniques, the so-called *projection* methods are worth to be recalled. In these regularization methods, the dimensionality of the space of the unknowns is reduced by choosing a suitable representation basis. In fact, a necessary (still not sufficient) condition to overcome ill-posedness is that the dimension of the space where the unknown function is looked for is not greater than the one of the data space [21]. Some examples can be found in [21, 31–34], wherein projection methods based on Fourier harmonics or Wavelet transform are adopted.

3. NEW ESTIMATION OF EPS VIA MRI/CT BASED PROJECTION

In the current state of the art, the electromagnetic model of the human body is built by segmenting MRI or CT images and associating to each thus identified tissue the relevant *ex-vivo* EPs value as given in

available databases [6, 7]. While still taking advantage from the same segmentation, which is nowadays a well assessed and effective procedure in the clinical practice [7], the proposed approach just exploits it to introduce a convenient expansion of the contrast function.

To illustrate this concept, let T be the number of tissues arising from the image segmentation. Then, a *tissue space* for the segmented scenario is introduced as the set of T functions, $\mathcal{T}_1, \ldots, \mathcal{T}_T$, such that the generic tissue basis function $\mathcal{T}_n$ is equal to one in all pixels associated with the n-th tissue and zero elsewhere. Accordingly, in order to deal with ill-posedness, the unknown contrast function can be expanded onto such a tissue space as:

$$\chi\left(\mathbf{r}\right) = \sum_{n=1}^{T} \hat{\chi}_n \mathcal{T}_n\left(\mathbf{r}\right) = \mathcal{T}(\hat{\chi}) \tag{3}$$

Equation (3) introduces a new way to approach to the problem of EPs estimation by microwave imaging, as it allows to associate to each tissue just a complex number, which represents its effective EPs. By doing so, high flexibility to deal with heterogeneous anthropomorphic scenarios made up of many tissues is guaranteed. Moreover, unlike approaches in [23–25], regularization in Eq. (3) does not require the selection of regularization parameters and allows a drastic reduction of the number of unknowns. Thanks to this patient specific tissue projection, the inverse scattering problem associated to EPs estimation can be cast as the solution of Eqs. (1)–(2), having as unknowns the T (complex) expansion coefficients $\hat{\chi}_1, \ldots, \hat{\chi}_T$, which encode the effective tissue EPs. In such a way, the complexity of the inverse problem is remarkably simplified, as only T complex unknowns have to be determined, with a significant mitigation of the ill-posedness and non-linearity of problem [16, 17, 21].

By means of the representation in Eq. (3), the EPs distribution is approximated with a step-wise constant function, rather than representing by punctual values within each tissue. Note that in case of small errors in the definition of T_n from the MRI or CT images, small errors on the effective EPs values are also expected, as proved in [25].

Obviously, the tissue projection in Eq. (3) derived by MRI or CT can be used in conjunction with many different inversion techniques. Also, the very low number of parameters one is looking for would enable a fruitful exploitation of global optimization techniques. Hence, by paying the price of an increased computational burden, a kind of completely "blind" retrieval procedure (but for the boundaries) is also possible.

However, in the following, by taking advantage of the analysis in [21], a local optimization procedure has been used. In this respect, the CSI [22] and Newton-Kantorovich (NK) inversion schemes [35] are probably the most popular inversion methods which allow to tackle the problem in its full non-linearity. However, NK aims at solving the inverse problem through a sequence of linearized problems (each having its range of validity), which require to solve a forward scattering problem at each step. This circumstance has a huge impact in term of computational burden. Conversely, by acting contemporarily on both Eqs. (1) and (2), the CSI method does not require to solve a forward problem at each iteration and does not involve any kind of approximations. For the above circumstances, in the following a CSI scheme has been adopted. In particular, the unknown χ and the auxiliary one W are simultaneously estimated by minimizing a cost functional [18, 32], which considers both the misfit in the *data* Eq. (1) and the one in the *state* Eq. (2), i.e.:

$$\Phi\left(W, \chi\right) = \sum_t \frac{\left\|\chi E_i\left(\mathbf{r_t}\right) + \chi \mathcal{A}_i\left[W\left(\mathbf{r_t}\right)\right] - W\left(\mathbf{r_t}\right)\right\|_{l_2}^2}{\left\|E_i\left(\mathbf{r_t}\right)\right\|_{l_2}^2} + \sum_t \frac{\left\|E_s\left(\mathbf{r_m}, \mathbf{r_t}\right) - \mathcal{A}_e\left[W\left(\mathbf{r_t}\right)\right]\right\|_{l_2}^2}{\left\|E_s\left(\mathbf{r_m}, \mathbf{r_t}\right)\right\|_{l_2}^2} \tag{4}$$

where the dependence from $\mathbf{r}$ has been omitted for the sake of brevity. Details about implementation of tissue basis representation in Eq. (3) in the framework of CSI gradient-based optimization are given in the Appendix.

To further improve the effectiveness of the procedure, additional information (other than spatial priors, such as for example physical feasibility of the achieved EP values [26]) can be exploited. Enforcing these latter can be eventually achieved by modifying the functional to be minimized by adding suitable penalty terms. In the following we have added a penalty term which restrict the admissible solutions to those with positive permittivity and conductivity, that is:

$$\Phi_P\left(\chi\right) = k_p \left\|\chi\left(\mathbf{r}\right) - P(\chi\left(\mathbf{r}\right))\right\|_{l_2}^2 \tag{5}$$

where $P(\cdot)$ is the projection of χ (and so $\hat{\chi}$) onto the set of positive functions [36], while k_p is a positive weight coefficient. In particular, at each iteration, $P(\chi)$ is updated in such a way that $P(\chi) = \chi$ in those pixels where permittivity and conductivity are positive, $P(\chi) = \mathrm{Re}(\chi)$ in those pixels where conductivity is negative, $P(\chi) = \mathrm{Im}(\chi)$ in those pixels where permittivity is negative, and $P(\chi) = 0$ elsewhere. By means of this projection, the minimization of the cost functional discards solutions with both negative permittivity and conductivity values. Concerning the choice of k_p, supported by an extensive numerical analysis, the penalty term (5) has been normalized to the number T of basis functions and the number of adopted antennas.

4. NUMERICAL ANALYSIS

A numerical analysis is now provided to assess the proposed strategy. The considered scenario is the head and neck region, which is both challenging from a morphologic point of view, as it is made up by many different tissues, and clinically relevant, being related to an increasingly important application of hyperthermia [37]. The estimation of the EPs in H&N region is discussed in the following, whereas the exploitation of the achieved EPs map in HTP is discussed in Section 5.

4.1. Description of the Testbed

As the main point of the paper is to present the basic idea of the method and assess it in controlled conditions before performing an experimental validation, in the following a numerical phantom is considered. In particular, an H&N voxel model has been obtained by merging the morphological information gathered from the high-resolution voxel-based anthropomorphic phantom in [38] with the results from *ex-vivo* tissue dielectric spectroscopy in [39, 40]. In doing so, we have carried out an accurate survey of works published in literature concerning the expected differences between *ex-vivo* and *in-vivo* EPs. Some of them claim that (at the considered frequency range) in living organism the permittivity is about 25% and the conductivity is about 30% higher that the related *ex-vivo* values [8–10]. For this reason, in order to build a numerical model (acting as a reference 'ground truth') such to be aligned with the supposed state of the art, we have associated to each tissue a value of the inherent effective EPs correspondingly increased with respect to the tabulated *ex-vivo* ones. Finally, to deal with a more realistic scenario, namely a non-exactly stepwise constant profile, the EPs in each voxel of the model have been perturbed by a $\pm 10\%$ uniformly distributed random fluctuation.

Two different transversal slices of the so-obtained H&N voxel model have been considered (slices A and B). In both of them, a circular inclusion of radius 0.014 m has been inserted to simulate a wide-spread oropharynx tumor [37] (see Fig. 1).

Following [27], the working frequency has been selected equal to 434 MHz and water has been considered as matching medium (relative permittivity 78 and conductivity 0.04 S/m). The entire region of interest has size 0.2295 m, and a discretization of 64×64 cells has been considered.

The data have been simulated by using a full-wave forward simulator based on the method of moments and, by following the model described in [41], corrupted with a complex random Gaussian noise $N(\mathbf{r_m}, \mathbf{r_t})$ with a given SNR. Three different level of SNR have been superimposed to the simulated data to assess the technique against the measurement uncertainties. Moreover, for the sake of a more realistic noise modeling, different realizations of noise for each SNR value (i.e., different random stream handle) have been considered to generate normal random noise samples. A set of incident fields radiated by N_A antennas, which act both as transmitters and receivers and are modelled as line sources, has been considered evenly spaced on a circumference with radius of 0.15 m, in agreement with the size of the applicators described in [27]. In particular, to evaluate the robustness against the reduction of the number of data, three different number N_A of antennas have been considered ($N_A = 28$, 20 and 12).

Concerning the initialization of the CSI procedure, different random starting guesses have been considered, without observing significant differences in terms of accuracy of EPs reconstructions. However, in order to reduce the computational time, the CSI procedure has been initialized by setting the coefficients $\hat{\chi}_n$ with the *ex-vivo* properties of the H&N tissues [39, 40]. Finally, the $\mathcal{T}_n$ basis functions have been defined starting from the voxel-based phantom exploited to build the model [38]. The accuracy
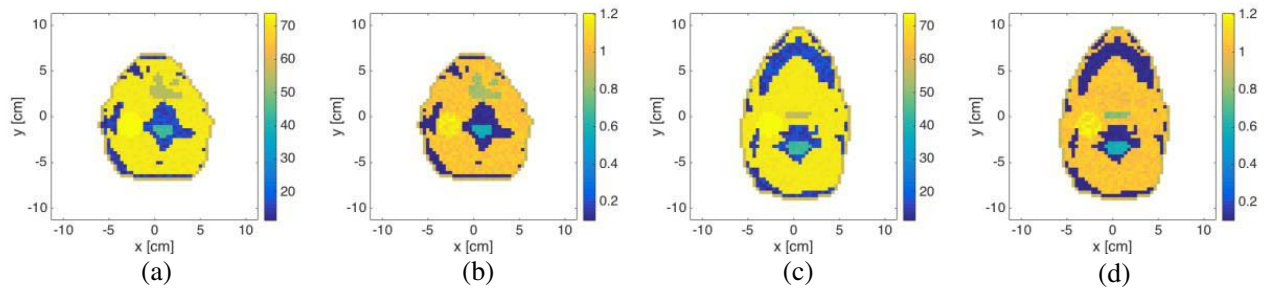
Figure 1. Relative permittivity and conductivity distributions of reference profiles: slice A (a)–(b), slice B (c)–(d).

of the retrieved EPs has been appraised through the normalized mean square error:

$$err = \frac{\left\| \epsilon_{s,n} - \tilde{\epsilon}_{s,n} \right\|_{l_2}^2}{\left\| \epsilon_{s,n} \right\|_{l_2}^2} \tag{6}$$

where $\epsilon_{s,n}$ is the actual complex permittivity of the n-th tissue, and $\tilde{\epsilon}_{s,n}$ is the estimated value.

4.2. Results and Discussion

In Figs. 2 and 3 the retrieved values of relative permittivity and conductivity for slices A and B are reported, respectively. As can be seen, the estimation of the EPs is extremely accurate, thanks to the MRI/CT-based basis representation in Eq. (3) composed of $T = 7$ and 8 tissues, for slice A and B respectively. The corresponding mean square errors, reported in Table 1, are much lower than the one corresponding to the starting guess (about 0.045 for both slices). It is important to note that good performance is also obtained when a higher amount of noise is superimposed on simulated data and a reduced number of antennas is considered. Such a reduction corresponds to a significant lowering in terms of the collected independent data. In particular, $N_A = 12$ sources correspond to 78 independent data (including the monostatic data), which is less than the actual degrees of freedom of the original problem [42].

Table 1. Mean square errors — Slice A and B.

N_A	SNR	SLICE A		SLICE B	
		err	Figures	*err*	Figures
28	30	0.0032		0.0030	
	20	0.0056	2(a)–(b)	0.0069	3(a)–(b)
	15	0.0094		0.0136	
20	30	0.0042		0.0029	
	20	0.0097	2(c)–(d)	0.0073	3(c)–(d)
	15	0.0147		0.0150	
12	30	0.0045		0.0030	
	20	0.0131	2(e)–(f)	0.0089	3(e)–(f)
	15	0.0172		0.0180	

In order to better understand the limitations of the technique, we have also considered a further reduction of the number of sensors up to the number of the tissue coefficients T. As can be observed from the mean square errors reported in Table 2 for slice A, the proposed approach still works fine with few antennas, provided a price can be paid in terms of required accuracy on measurements (in other

Table 2. Mean square errors — Slice A: Further reduction of the number of sensors.

N_A	SNR	err	Figures
10	50	0.0044	
	40	0.0048	
	30	0.0065	-
	20	0.0135	
	15	0.0400	
7	50	0.0063	
	40	0.0102	
	30	0.0151	-
	20	0.0179	
	15	0.0401	
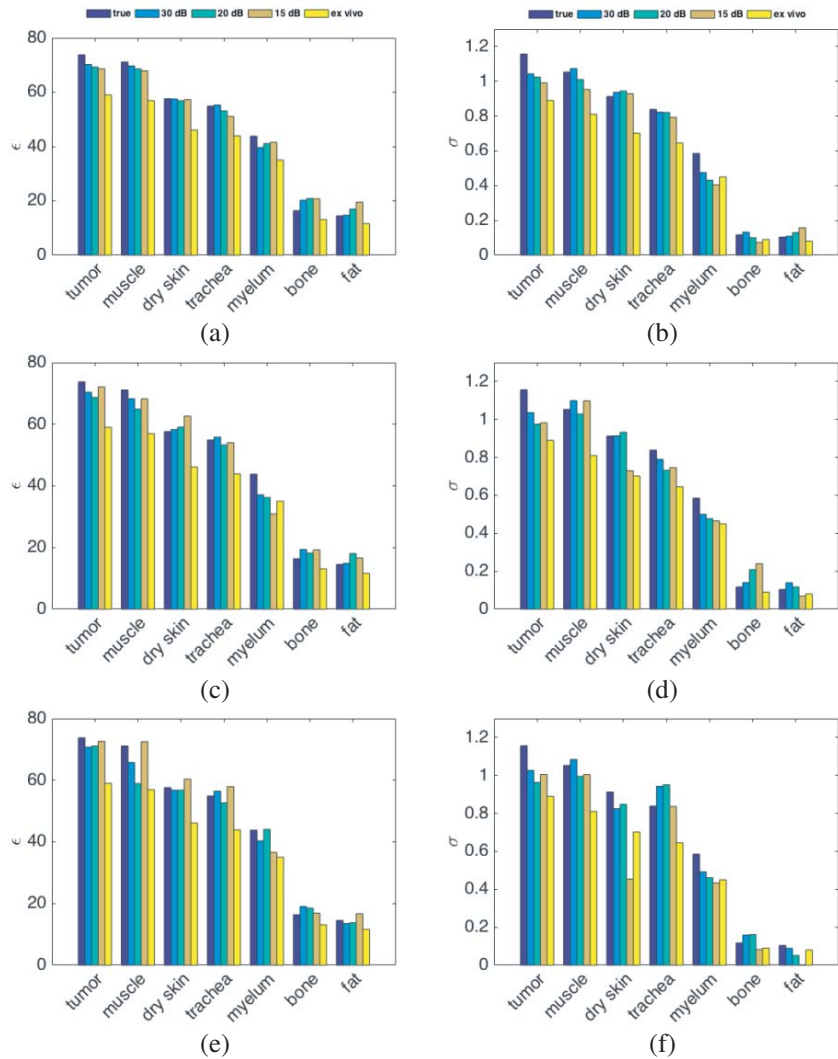
Figure 2. EPs Estimation-slice A: Retrieved values of relative permittivity and conductivity corresponding to $N_A = 28$ (a)–(b), $N_A = 20$ (c)–(d) and $N_A = 12$ (e)–(f).
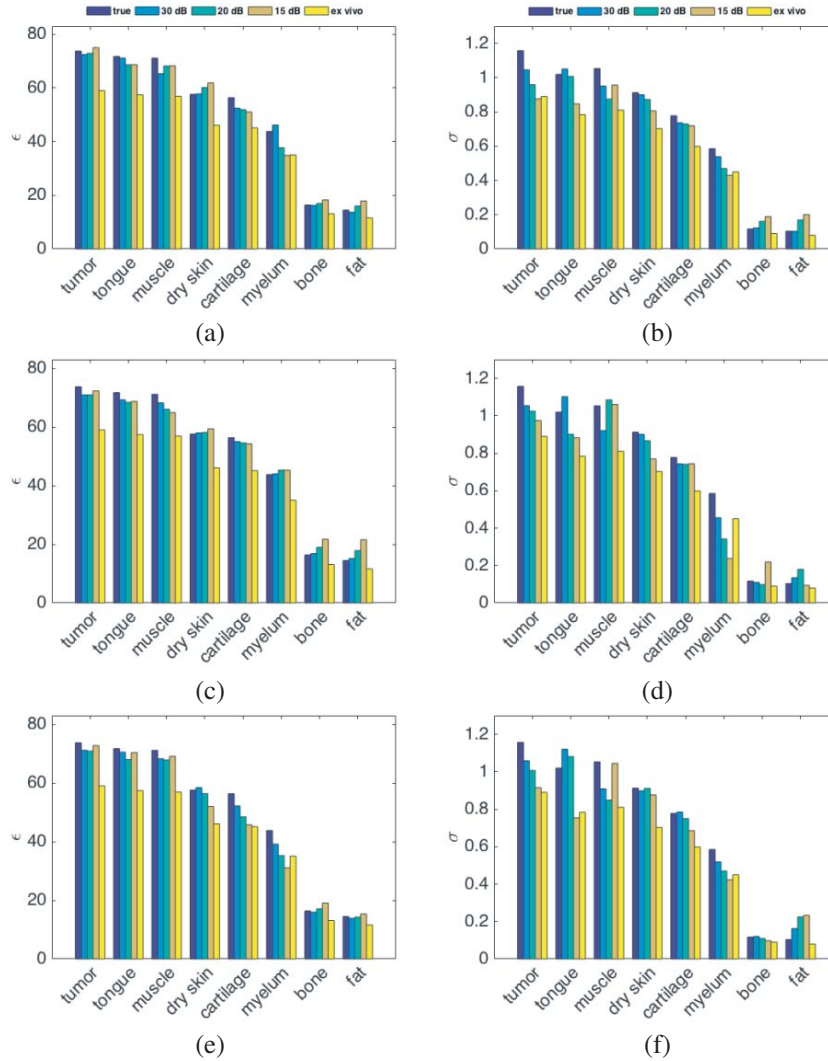
Figure 3. EPs Estimation-slice B: Retrieved values of relative permittivity and conductivity corresponding to $N_A = 28$ (a)–(b), $N_A = 20$ (c)–(d) and $N_A = 12$ (e)–(f).

words, the number of sensors can be lowered provided measurements are more and more accurate). For the sake of brevity, the corresponding EPs reconstructions are not shown.

5. A CASE OF INTEREST: IMPACT ON HYPERTHERMIA TREATMENT PLANNING

This section aims at evaluating the impact of the introduced EPs estimation technique when dealing with the planning of a hyperthermia treatment. In such application, the proposed technique appears to be particularly advantageous as it allows to exploit the hyperthermia antennas not only to deliver the treatment, but also as a sensing system to perform the MWT of the scenario.

Hyperthermia takes place when a supra-physiologic temperature increase (40–44°C) is selectively applied to the tumor for a certain time (60–90 min). As a matter of fact, in order to uniformly shape the temperature over a given target area while avoiding the occurrence of possible hot-spots in healthy tissues, HTP requires both an accurate knowledge of patient-specific EPs and an effective strategy to optimally determine the excitations of the antennas constituting the applicator, which is supposed to be a phased array.

In view of temperature measurement difficulties, optimization of the heating for phased array applicators relies on HTP, especially in the H&N region [43]. The herein adopted optimization strategy is focusing via constrained power optimization (FOCO) procedure [30], which maximizes the power deposition in the target volume, while constraining it below given levels in healthy tissues, thus avoiding hot spots. Thanks to its mathematical formulation, FOCO is faster and more stable than other optimization strategies [2, 44], since it is based on solving one (or more) convex optimization problems (see [30] for more details).
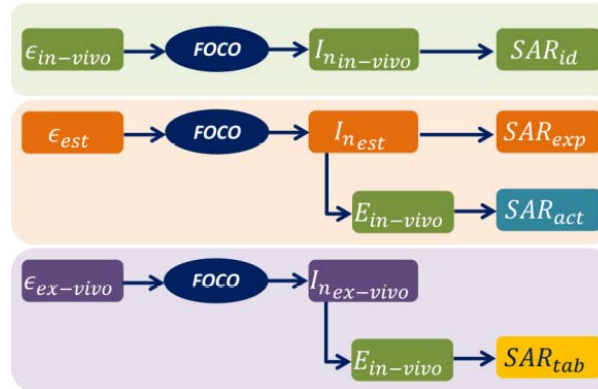

Figure 4. Schematic view of the adopted evaluation setup.

In order to fully understand the importance of a reliable knowledge of the patient-specific EPs and assess the effective improvements achieved by means of the proposed *in-vivo* estimation technique, four different cases, as shown in Fig. 4, have been considered. In particular, we have considered the focused SAR distributions obtained by:

(i)   assuming the exact knowledge of the actual *in-vivo* parameters, say SAR_{id};

(ii) considering the EM parameters estimated by means of the proposed technique, say SAR_{exp};

(iii) applying the complex excitation coefficients obtained in (ii) to the actual *in-vivo* field distribution, say SAR_{act};

(iv) applying the complex excitation coefficients designed according to the *ex-vivo* EPs [39, 40] to the actual *in-vivo* field distribution, say SAR_{tab}.

For the sake of a better understanding, let us note that SAR_{id} can be seen as a kind of ideal ultimate performance that one can achieve, whereas the SAR_{tab} represents what is nowadays achieved by the currently used HTP procedures exploiting the tabulated *ex-vivo* parameters [39, 40]. SAR_{exp} is the SAR distribution which is expected to be actually induced in the patient on the basis of the developed EPs estimation strategy. Finally, SAR_{act} is the power deposition administered by exploiting the complex excitation coefficients computed on the basis of the estimated EPs parameters in the actual scenario (e.g., including fluctuations inside each tissue, as described in Subsection 4.1). Accordingly, planning a treatment by exploiting the estimated EPs yields accurate and effective results as long as the estimated power depositions SAR_{exp} is similar to both SAR_{act} and SAR_{id} (this latter is considered as a benchmark when *in-vivo* EPs are fully known).

Figures 5 and 6 depict the SAR_{id}, SAR_{exp}, SAR_{act} and SAR_{tab} distributions for slices A and B corresponding to a 20 array element configuration and an SNR equal to 20 dB. From a qualitative point of view, SAR_{id}, SAR_{exp}, SAR_{act} are quite similar, while SAR_{tab} shows an undesired heating of the tissue outside the tumor. In addition, it is also possible to appreciate that SAR_{tab} exhibits a slight "mis-coverage" of the target area as compared to the others SAR distributions. This result suggests that the electromagnetic model obtained by means of the MRI/CT-based EPs retrieval procedure allows a better design of the antenna array excitations than the *ex-vivo* model [39, 40].

For the sake of a quantitative comparison, two different metrics have been adopted, i.e., a modified version of the Target to Hot-Spot Quotient (mTHQ) [45] and the maximum SAR side peak (SSP) in
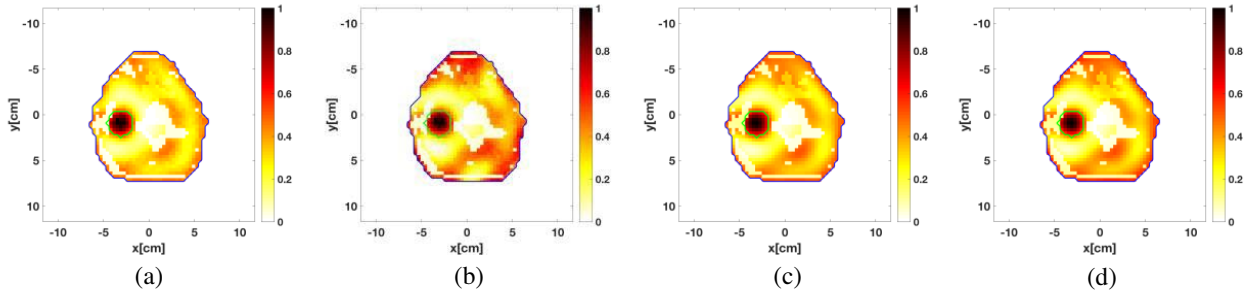
Figure 5. SAR distributions as described in (i)–(iv) points, related to slice A with 20 array elements and SNR equal to 20 dB. (a) SAR id. (b) SAR tab. (c) SAR exp. (d) SAR act.

Figure 6. SAR distributions as described in (i)–(iv) points, related to slice B with 20 array elements and SNR equal to 20 dB. (a) SAR id. (b) SAR tab. (c) SAR exp. (d) SAR act.
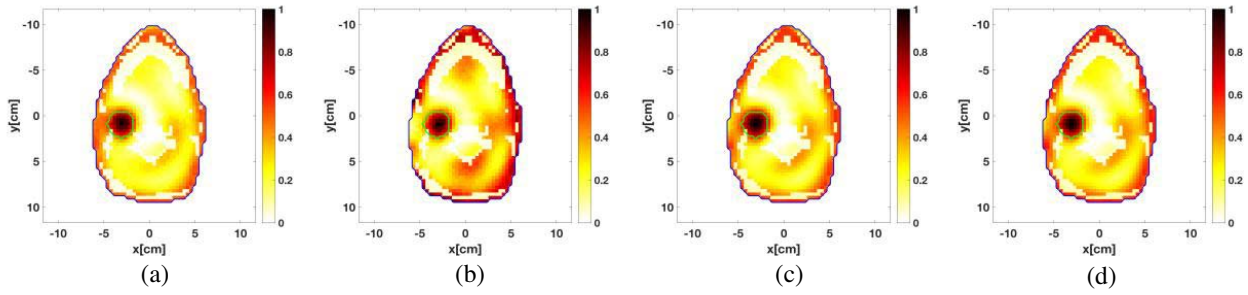
healthy tissues [3]. The mTHQ is an adapted version of the metric presented in [45] to deal with the 2D case at hand. It is defined as the ratio of the average SAR within the target area and the average SAR in the healthy tissues. Tables 3 and 4 report the SSP and mTHQ values for slice A and B, respectively, evaluated on the SAR distributions (i)–(iv) for the considered array configurations and noise levels. Interestingly, these synthetic parameters clearly indicate that the proposed EPs estimation approach allows to improve the performance obtainable with respect to the nowadays used HTP procedures based on *ex-vivo* EPs parameters [39, 40].

The trends shown in Tables 3 and 4 can be analyzed from a twofold prospective. For a given noise level, both mTHQ and SSP values related to SAR (i)–(iii) increasingly diverge when decreasing N_A.

Table 3. Evaluation of SSP and THQ Metrics related to slice A.

N_A	SNR	SSP [%]				mTHQ [-]			
		SAR_{id}	SAR_{exp}	SAR_{act}	SAR_{tab}	SAR_{id}	SAR_{exp}	SAR_{act}	SAR_{tab}
	30dB		50	53			10.08	9.73	
28	20dB	47	52	58	89	10.50	9.96	9.22	9.33
	15dB		52	63			9.68	8.52	
	30dB		50	52			9.94	9.78	
20	20dB	47	51	59	79	10.54	9.89	9.30	9.02
	15dB		48	54			10.33	9.84	
	30dB		53	55			10.75	10.49	
12	20dB	50	57	65	76	11.12	10.72	9.87	9.15
	15dB		49	65			10.94	9.37	

Table 4. Evaluation of SSP and THQ Metrics related to slice B.

N_A	SNR	SSP [%]				mTHQ [-]			
		SAR_{id}	SAR_{exp}	SAR_{act}	SAR_{tab}	SAR_{id}	SAR_{exp}	SAR_{act}	SAR_{tab}
28	30dB		57	62			3.21	3.00	
	20dB	54	57	69	98	3.34	3.13	2.73	2.41
	15dB		55	79			3.06	2.44	
20	30dB		57	60			3.23	3.15	
	20dB	54	57	63	98	3.36	3.22	3.06	2.45
	15dB		55	67			3.27	2.91	
12	30dB		58	58			3.31	3.29	
	20dB	54	58	63	88	3.34	3.40	3.22	2.55
	15dB		53	70			3.73	3.20	

The same behavior can be observed, for a fixed N_A when the noise level is increased. This means that the SAR_{act}, i.e., the actual *in-vivo* performance, is different from the ideal one, due to the increased error on the estimated EPs. Although this circumstance, both mTHQ and SSP corresponding to the SAR_{act} are generally better than the one corresponding to SAR_{tab}. This confirms the importance of a reliable knowledge of the patient-specific EPs. Results are also consistent with FOCO robustness to EPs uncertainty as discussed in [30].

6. CONCLUSIONS

In this paper, a new approach to perform the estimation of effective EPs of biological tissues has been proposed, described and tested in controlled conditions. The approach benefits from MWT and medical images derived from MRI or CT. Differently from other approaches in literature, it considers hard spatial priors derived from the MRI or CT segmented images in such a way to better represent the unknown EPs. As such, the technique exhibits high flexibility, wide applicability, as well as high accuracy in the determination of the effective EPs, as shown in the numerical analysis. The tissue projection has been herein proposed within a CSI scheme, but it can be used in conjunction with other inversion techniques.

The approach has been assessed and tested against a 2D realistic and anthropomorphic H&N scenario, and an extensive analysis has been performed by varying the amount of noise on the data and the number of antennas. By doing so, the exact knowledge of the tissues boundaries is assumed. In case of uncertainties on the spatial priors, the boundary of the reconstructed EPs could be eventually corrected by successively exploiting the binary regularization described in [46]. However, note that small errors in the spatial priors are not expected to significantly affect the effective EPs reconstructions [23–25] and hence the performance of the therapeutic treatments or dose estimations [30].

Finally, being the knowledge of EPs relevant in the determination of SAR distributions, HTP has been considered as a case of interest and the impact of the introduced estimation technique has been evaluated. In particular, the obtained performance has been compared with respect to the one reached in case of HTP based on *ex-vivo* model. The results confirm that the improved knowledge of the effective EPs implies a better design of the heating system and a better control of the occurrence of undesired effects outside the tumors.

Future work will be devoted at extending and testing the method in the more challenging 3D vector scenario and against experimental data.

APPENDIX A.

In this section, the expressions of the gradient and the line search parameter related to the cost functional (4) in a CSI conjugate gradient scheme are reported. To this end, let us denote with $\mathcal{T}^{-1}$ the operator which transform the contrast function from pixels to tissue space coefficients and with $\mathcal{T}$ the operator which works on the coefficients and returns a pixel representation. The expression of the cost functional can be rewritten as follows:

$$\Phi(W, \hat{\chi}) = \sum_t \frac{\left\|\mathcal{T}(\hat{\chi})E_i + \mathcal{T}(\hat{\chi})\mathcal{A}_i[W] - W\right\|_{l_2}^2}{\|E_i\|_{l_2}^2} + \sum_t \frac{\|E_s - \mathcal{A}_e[W]\|_{l_2}^2}{\|E_s\|_{l_2}^2} \tag{A1}$$

where the dependence from $\mathbf{r}$, $\mathbf{r_t}$ and $\mathbf{r_m}$ has been omitted for the sake of brevity.

Concerning the second term in Eq. (A1) both the expression of the gradient and the coefficients of the algebraic polynomial for the determination of the step length are as in [21, 32]. On the contrary, following [21, 32], the expression of the gradients with respect $\hat{\chi}$ reads:

$$\nabla\Phi_{\hat{\chi}} = 2\sum_t \frac{\mathcal{T}^{-1}\left[(E_i + \mathcal{A}_i[W])^* m_s\right]}{\|E_i\|_{l_2}^2} \tag{A2}$$

where $m_s = \mathcal{T}(\hat{\chi})E_i + \mathcal{T}(\hat{\chi})\mathcal{A}_i[W] - W$ represents the misfit about the state equation, and the superscript * denotes the complex conjugate operation.

Let us consider the behavior of functional (A1) along an arbitrary line given by $W + \lambda\Delta W$ and $\hat{\chi} + \lambda\Delta\hat{\chi}$, where ΔW and $\Delta\hat{\chi}$ represent the descent research directions considered at a generic iteration. Due to the nature of the involved operator, this latter can be rewritten as a fourth-degree algebraic polynomial, i.e.:

$$\Phi(W + \lambda\Delta W, \hat{\chi} + \lambda\Delta\hat{\chi}) = a\lambda^4 + b\lambda^3 + c\lambda^2 + d\lambda + e \tag{A3}$$

where:

$$a = \sum_t \frac{\|\mathcal{T}(\Delta\hat{\chi})\mathcal{A}_i[\Delta W]\|_{l_2}^2}{\|E_i\|_{l_2}^2}$$

$$b = 2\text{Re}\sum_t \frac{\langle\mathcal{T}(\Delta\hat{\chi})\mathcal{A}_i[\Delta W], \Delta m_s\rangle}{\|E_i\|_{l_2}^2}$$

$$c = \sum_t \frac{\|\Delta m_s\|_{l_2}^2}{\|E_i\|_{l_2}^2} + 2\text{Re}\sum_t \frac{\langle\mathcal{T}(\Delta\hat{\chi})\mathcal{A}_i[\Delta W], m_s\rangle}{\|E_i\|_{l_2}^2}$$

$$d = 2\text{Re}\sum_t \frac{\langle m_s, \Delta m_s\rangle}{\|E_i\|_{l_2}^2} \qquad e = \sum_t \frac{\|m_s\|_{l_2}^2}{\|E_i\|_{l_2}^2}$$

$\Delta m_s = \mathcal{T}(\Delta\hat{\chi})(E_i + \mathcal{A}_i[W]) + \mathcal{T}(\hat{\chi})\mathcal{A}_i[\Delta W] - \Delta W$ and $\text{Re}(\cdot)$ extracts the real part of the argument.

ACKNOWLEDGMENT

REFERENCES

1. Durney, C. H., "Electromagnetic dosimetry for models of humans and animals: A review of theoretical and numerical techniques," *Proceedings of the IEEE*, Vol. 68, No. 1, 33–40, 1980.

2. De Greef, M., H. P. Kok, D. Correia, A. Bel, and J. Crezee, "Uncertainty in hyperthermia treatment planning: The need for robust system design," *Phys. Med. Biol.*, Vol. 56, No. 11, 3233–3250, 2011.

3. Bellizzi, G. G., L. Crocco G. M. Battaglia, and T. Isernia, "Multi-frequency constrained SAR focusing for patient specific hyperthermia treatment," *IEEE JERM*, Vol. 1, No. 2, 74–80, 2017.

4. Bellizzi, G. G., D. A. M. Iero, L. Crocco, and T. Isernia, "3-D field intensity shaping: The scalar case," *IEEE Ant. and Wir. Prop. Letters*, 2018.

5. Chow, E. Y., C. L. Yang, Y. Ouyang, A. L. Chlebowski, P. P. Irazoqui, and W. J. Chappell, "Wireless powering and the study of RF propagation through ocular tissue for development of implantable sensors," *IEEE Trans. on Antennas and Propag.*, Vol. 59, No. 6, 2379–2387, 2011.

6. Gabriel, S., R. W. Lau, and C. Gabriel, "The dielectric properties of biological tissues: II. Measurements in the frequency range 10 Hz to 20 GHz," *Phys. Med. Biol.*, Vol. 41, 2251–2269, 1996.

7. Fortunati, V., R. F. Verhaart, F. van der Lijn, W. J. Niessen, J. F. Veenland, M. M. Paulides, and T. van Walsum, "Tissue segmentation of head and neck CT images for treatment planning: A multi-atlas approach combined with intensity modeling," *Med. Phys.*, Vol. 7, No. 40, 2013.

8. Halter, R. J., T. Zhou, P. M. Meaney, A. Hartov, R. J. Barth Jr., K. M. Rosenkranz, W. A. Wells, C. A Kogel, A. Borsic, E. J. Rizzo, and K. D. Paulsen, "The correlation of in-vivo and ex-vivo tissue dielectric properties to validate electromagnetic breast imaging: initial clinical experience," *Physiol. Meas.*, Vol. 30, No. 6, S121, 2009.

9. O'Rourke, A. P., M. Lazebnik, J. M. Bertram, M. C. Converse, S. C. Hagness, J. G. Webster, and D. M. Mahvi, "Dielectric properties of human normal, malignant and cirrhotic liver tissue: in-vivo and ex-vivo measurements from 0.5 to 20 GHz using a precision open-ended coaxial probe," *Phys. Med. Biol.*, Vol. 52, 4707–19, 2007.

10. Salahuddin, S., A. La Gioia, M. A. Elahi, E. Porter, M. O'Halloran, and A. Shahzad, "Comparison of in-vivo and ex-vivo dielectric properties of biological tissues," *International Conference on Electromagnetics in Advanced Applications*, 582–585, 2017.

11. Haemmerich, D., O. R. Ozkan, J. Z. Tsai, S. T. Staelin, S. Tungjitkusolmun, D. M. Mahvi, and J. G. Webster, "Changes in electrical resistivity of swine liver after occlusion and postmortem," *Med. Biol. Eng. Comput.*, No. 40, 29–33, 2002.

12. Meaney, P. M., T. Zhou, D. Goodwin, A. Golnabi, E. A. Attardo, and K. D. Paulsen, "Bone dielectric property variation as a function of mineralization at microwave frequencies," *International Journal of Biomedical Imaging*, Vol. 2012, Article ID 649612, 9 pages, 2012.

13. Gabriel, C. and A. Peyman, *Chapter 69 — Dielectric Properties of Biological Tissues; Variation with Age*, Editors, Jeffrey L. Ram, P. Michael Conn, Conn's Handbook of Models for Human Aging, 2nd Edition, 939–952, Academic Press, 2018.

14. Haacke, E. M., L. S. Petropoulos, E. W. Nilges, and D. H. Wu, "Extraction of conductivity and permittivity using magnetic resonance imaging," *Phys. Med. Biol.*, Vol. 36, 723–34, 1991.

15. Katscher, U. and C. A. Berg, "Electric properties tomography: Biochemical, physical and technical background, evaluation and clinical applications," *NMR in Biomedicine*, 2017.

16. Colton, D. and R. Kress, *Inverse Acoustic and Electromagnetic Scattering Theory*, Springer-Verlag, Berlin, Germany, 1998.

17. Bertero, M. and P. Boccacci, "Introduction to inverse problems in imaging," *Institute of Physics*, Bristol, UK, 1998.

18. Catapano, I., L. Di Donato, L. Crocco, O. M. Bucci, A. F. Morabito, T. Isernia, and R. Massa, "On quantitative microwave tomography of female breast," *Progress In Electromagnetics Research*, Vol. 97, 75–93, 2009.

19. Bai, F., A. Franchois, and A. Pizurica, "3D microwave tomography with huber regularization applied to realistic numerical breast phantoms," *Progress In Electromagnetics Research*, Vol. 155, 75–91, 2016.

20. Baran, A., D. J. Kurrant, A. Zakaria, E. C. Fear, and J. LoVetri, "Breast imaging using microwave tomography with radar-based tissue-regions estimation," *Progress In Electromagnetics Research*, Vol. 149, 161–171, 2014.

21. Isernia, T., V. Pascazio, and R. Pierri, "On the local minima in a tomographic imaging technique," *IEEE Trans. on Geosci. and Remote Sens.*, Vol. 39, No. 7, 1596–1607, Jul. 2001.

22. Van den Berg, P. M. and R. E. Kleinman, "A contrast source inversion method," *Inverse Problems*, Vol. 13, 1607–1620, 1997.

23. Golnabi, A., et al., "3D microwave tomography of the breast using prior anatomical information," *Med. Phys.*, Vol. 43, No. 4, 1933–1944, 2016.

24. Meaney, P., et al., "Integration of microwave tomography with magnetic resonance for improved breast imaging," *Med. Phys.*, Vol. 40, No. 10, 2013.

25. Neira, L. M., et al., "High-resolution microwave breast imaging using a 3-D inverse scattering algorithm with a variable-strength spatial prior constraint," *IEEE Trans. Antennas Propag.*, Vol. 65, No. 11, 6002–6014, 2017.

26. Rahimov, A., A. Litman, and G. Ferrand, "MRI-based electric properties tomography with a quasi-Newton approach," *Inverse Problems*, Vol. 33, No. 10, 2017.

27. Rijnen, Z., P. Togni, R. Roskam, S. G. Van De Geer, R. H. Goossens, and M. M. Paulides, "Quality and comfort in head and neck hyperthermia: A redesign according to clinical experience and simulation studies," *Int. J. Hyperthermia*, Vol. 31, No. 8, 823–830, 2017.

28. Paulides, M. M., R. M. C. Mestrom, G. Salim, B. B. Adela, W. C. M. Numan, T. Drizdal, D. T. B. Yeo, and A. B. Smolders, "A printed Yagi-Uda antenna for application in magnetic resonance thermometry guided microwave hyperthermia applicators," *Phys. Med. Biol.*, Vol. 62, No. 5, 1831–1847, 2017.

29. Gellermann, J., W. Wlodarczyk, A. Feussner, H. Fähling, J. Nadobny, B. Hildebrandt, R. Felix, and P. Wust, "Methods end potentials of magnetic resonance imaging for monitoring radiofrequency hyperthermia in a hybrid system," *Int. J. Hyperthermia*, Vol. 21, No. 6, 497–513, 2005.

30. Iero, D. A., L. Crocco, and T. Isernia, "Thermal and microwave constrained focusing for patient-specific breast cancer hyperthermia: A robustness assessment," *IEEE Trans. Antennas Propag.*, Vol. 62, No. 2, 814–821, 2014.

31. Li, M., O. Semerci, and A. Abubakar, "A contrast source inversion method in the wavelet domain," *Inverse Problems*, Vol. 29, No. 2, 1–19, 2013.

32. Bevacqua, M., L. Crocco, and T. Isernia, "Non-linear inverse scattering via sparsity regularized contrast source inversion," *IEEE Transactions on Computational Imaging*, Vol. 3, No. 2, 296–304, Jun. 2017.

33. Palmeri, R., M. T. Bevacqua, L. Crocco, T. Isernia, and L. Di Donato, "Microwave Imaging via Distorted Iterated Virtual Experiments," *IEEE Trans. on Antennas and Propag.*, Vol. 65, No. 2, 829–838, 2017.

34. Scapaticci, R., I. Catapano, and L. Crocco, "Wavelet-based adaptive multiresolution inversion for quantitative microwave imaging of breast tissues," *IEEE Trans. Antennas Propag.*, Vol. 60, No. 8, 3717–3726, 2012.

35. Roger, A., "Newton-Kantorovitch algorithm applied to an electromagnetic inverse problem," *IEEE Trans. Antennas Propag.*, Vol. 29, No. 2, 232–238, Mar. 1981

36. Bucci, O. M., I. Catapano, L. Crocco, and T. Isernia, "Synthesis of new variable dielectric profile antennas via inverse scattering techniques: A feasibility study," *IEEE Trans. Antennas Propag.*, Vol. 53, No. 4, 1287–1297, Apr. 2005.

37. Datta, N. R., S. Rogers, S. G. Ordonez, E. Puric, and S. Bodis, "Hyperthermia and radiotherapy in the management of head and neck cancers: A systematic review and meta-analysis," *Int. J. Hyperthermia*, Vol. 32, No. 1, 31–40, 2016.

38. Zubal, I., C. Harrell, E. Smith, Z. Rattner, G. Gindi, and P. Hoffer, "Computerized three-dimensional segmented human anatomy," *Med. Phys.*, Vol. 21, No. 2, 299–302, 1994.

39. Hasgall, P. A., F. D. Gennaro, C. Baumgartner, E. Neufeld, M. Gosselin, D. Payne, A. Klingenbock, and N. Kuster, "IT'IS Database for thermal and electromagnetic parameters of biological tissues," Version 3.0, 2015.

40. Andreuccetti, D., R. Fossi, and C. Petrucci, "An Internet resource for the calculation of the dielectric properties of body tissues in the frequency range 10 Hz–100 GHz, IFAC-CNR, Florence (Italy) — Based on data published by C. Gabriel et al. in 1996," Website at

http://niremf.ifac.cnr.it/tissprop/, 1997.

41. Tournier, P. H., M. Bonazzoli, V. Dolean, F. Rapetti, F. Hecht, F. Nataf, I. Aliferis, I. El Kanfoud, C. Migliaccio, M. de Buhan, et al., "Numerical modeling and high-speed parallel computing: New perspectives on tomographic microwave imaging for brain stroke detection and monitoring," *IEEE Ant. Prop. Magazine*, Vol. 59, No. 5, 98–110, Oct. 2017.

42. Bucci, O. M. and T. Isernia, "Electromagnetic inverse scattering: Retrievable nformation and measurement strategies," *Radio Sci.*, Vol. 32, 2123–2138, 1997.

43. Wust, P., B. Hildebrandt, G. Sreenivasa, B. Rau, J. Gellermann, H. Riess, R. Felix, and P. M. Schlag, "Hyperthermia in combined treatment of cancer," *The Lancet Oncology*, Vol. 3, No. 8, 487–497, 2002.

44. Cappiello, G., B. Mc Ginley, M. A. Elahi, T. Drizdal, M. M. Paulides, M. Glavin, M. O'Halloran, and E. Jones, "Differential evolution optimization of the sar distribution for head and neck hyperthermia," *IEEE Trans. Bio. Eng.*, Vol. 64, 1875–1885, Aug. 2017.

45. Canters, R. A. M., P. Wust, J. F. Bakker, and G. C. Van Rhoon, "A literature survey on indicators for characterization and optimization of SAR distributions in deep hyperthermia, a plea for standardization," *Int J Hyperthermia*, Vol. 25, 593–608, Nov. 2009.

46. Catapano, I., L. Crocco, and T. Isernia, "A simple two-dimensional inversion technique for imaging homogeneous targets in stratified media," *Radio Sci.*, Vol. 39, 2004.